Rock strength and structural controls on fluvial erodibility: implications for drainage divide mobility in a collisional mountain belt

Jesse R. Zondervan*, Martin Stokes, Sarah J. Boulton, Matt W. Telfer, Anne E. Mather

School of Geography, Earth and Environmental Sciences, University of Plymouth, Plymouth, PL4 8AA, United Kingdom

Correspondence to: Jesse R. Zondervan (jesse.zondervan@plymouth.ac.uk)

Highlights

- We estimate rock strength, erodibility and drainage divide mobility in the High Atlas Mountains
- The weakest rock-type in the High Atlas is up to two orders of magnitude more erodible than the strongest
- In gently deformed horizontal strata of the sedimentary cover the drainage divide is mobile
- Faulted and folded metamorphic sedimentary bedrock coincide with a stable drainage divide
- Exhumation of crystalline basement forces the drainage divide into the centre of exposed basement

Abstract

Numerical model simulations and experiments have suggested that when migration of the main drainage divide occurs in a mountain belt, it can lead to the rearrangement of river catchments, rejuvenation of topography, and changes in erosion rates and sediment flux. We assess the progressive mobility of the drainage divide in three lithologically and structurally distinct groups of bedrock in the High Atlas (NW Africa). The geological age of bedrock and its associated tectonic architecture in the mountain belt increases from east to west in the study area, allowing us to track both variations in rock strength and structural configuration which influence drainage mobility during erosion through an exhuming mountain belt. Collection of field derived

measurements of rock strength using a Schmidt hammer and computer based extraction of river channel steepness permit estimations of contrasts in fluvial erodibilities of rock types. The resulting difference in fluvial erodibility between the weakest and the strongest lithological unit is up to two orders of magnitude. Published evidence of geomorphic mobility of the drainage divide indicates that such a range in erodibilities in horizontal stratigraphy of the sedimentary cover may lead to changes in erosion rates as rivers erode through strata, leading to drainage divide migration. In contrast, we show that the faulted and folded metamorphic sedimentary rocks in the centre of the mountain belt coincide with a stable drainage divide. Finally, where the strong igneous rocks of the crystalline basement are exposed after erosion of the covering meta-sediments, there is a decrease in fluvial erodibility of up to a factor of three, where the drainage divide is mobile towards the centre of the exposed crystalline basement. The mobility of the drainage divide in response to erosion through rock-types and their structural configuration in a mountain belt has implications for the perception of autogenic dynamism of drainage networks and fluvial erosion in mountain belts, and the interpretation of the geomorphology and downstream stratigraphy.

Keywords: collisional mountain belt, drainage divide, rock strength, erodibility, High Atlas

6493 words (excl. highlights, abstract, tables, figure captions, author contributions, funding, refs)

1 Introduction

Collisional mountains form the erosional focus of the Earth's surface. The tectonic and climatic interpretation of mountain topography and depositional stratigraphy depends on understanding the dynamics of eroding bedrock rivers. The central drainage divide of a mountain belt is the topographic boundary between river catchments draining either flank. Any movement of the drainage divide can result in the rearrangement of catchments, rejuvenation of topography, and changes in erosion rates and sediment flux (Bonnet, 2009; Giachetta et al., 2014). Bedrock erodibility

52 is expected to play a significant role in drainage divide reorganisation since heterogeneous
53 exhumation of weak and strong substrates can enhance and suppress erosion respectively
54 (Giachetta et al., 2014; Gallen, 2018) and cause topographic rejuvenation, for example through the
55 exhumation of a basement palaeosurface (Strong et al., 2019). This is especially the case in post-
56 orogenic settings where erosion is dominant over crustal thickening (Gallen, 2018; Bernard et al.,
57 2019). However, the magnitude of erodibility variation within a mountain belt, and the mobility of
58 the drainage divide as rivers erode through its stratigraphy are still relatively unexplored.

59 Collisional orogens are characterised by bedrock rivers eroding through variable rock strength and
60 tectonic architectures, such as very strong crystalline basement, deformed strong meta-sediments,
61 and sedimentary cover composed of weak as well as stronger strata. Recent numerical modelling
62 studies show the complexity of incision into horizontal or gently dipping strata of varying erodibility
63 (Forte et al., 2016; Perne et al., 2017), and also suggest steady-state denudation is more likely to
64 develop in tilted and /or faulted strata that have been highly deformed (Forte et al., 2016). The
65 results of these models imply drainage mobility might be prevalent during incision in sedimentary
66 cover but not in more deformed components of a collisional mountain belt. In a field study, Gallen
67 (2018) modelled the erosion of a hard horizontal rock layer in the Appalachians. This model predicts
68 that a geologically instantaneous capture of the Upper Tennessee River catchment by the Lower
69 Tennessee River occurred at 9 Ma, which has led to a shift in the drainage divide and explains
70 observed subsequent topographic rejuvenation in the landscape visible today. In the Pyrenees,
71 Bernard et al. (2019) show the drainage divide follows the position of high-strength, high-elevation
72 plutons in the crystalline basement in the centre of the belt, suggesting a direct lithological control
73 on the position of the central drainage divide. These field studies demonstrate the drainage divide
74 can be mobile in near-horizontal sedimentary stratigraphy of mountain belts and is likely to move to
75 the centre of highly resistant plutons as they get exhumed in the axis of a collisional mountain belt.
76 However, both studies also demonstrate the challenge of documenting drainage mobility, which is
77 often only recognisable in instantaneous capture events which leave pervasive topographic

78 evidence. In addition, whilst numerical simulation studies are instrumental in predicting long-term
79 processes in geomorphology which are hard to derive from observations of modern day landscapes
80 alone, these involve simplifications and it is challenging to model the full complexity of lithologies
81 and structural geology of a collisional mountain belt. Furthermore, the fluvial erodibility of rock,
82 which depends on rock mass strength as well as jointing and weathering, is challenging to measure
83 quantitatively (Bursztyn et al., 2015) and consequently the range of erodibility inputs in modelling
84 studies vary widely (Roy et al., 2015; Forte et al., 2016; Yanites et al., 2017).

85 Consequently, while theory and numerical models predict a role for bedrock erodibility in driving
86 drainage divide mobility, where and when this is expected to occur in the evolution of mountain
87 belts needs to be understood from a range of settings with varying rock strength conditions. The
88 challenges of measuring and characterising bedrock erodibility (Bursztyn et al., 2015) and drainage
89 divide dynamics in field settings (Willett et al., 2014; Forte and Whipple, 2018) remain key problems.
90 Addressing this challenge requires a dataset on rock erodibility that is combined with topographic
91 measures of drainage divide mobility in a mountain belt where erosion is dominant over tectonic
92 advection, and where rivers erode through a lithologically variable landscape. In this study, we aim
93 to derive data and present it in a form that is useful for both field geologists and numerical
94 modellers alike. We focus our study on the central High Atlas Mountains (Fig. 1), where different
95 stages of orogenic landscape evolution, from erosion through gently dipping sedimentary cover to
96 exhumed crystalline basement occur along the length of the main drainage divide, forming a natural
97 experiment. Furthermore, the continental inland setting, low weathering rates associated with an
98 arid climate and low rates of tectonic activity make this post-orogenic mountain range an ideal
99 setting to study erodibility-induced drainage divide mobility. In this study, we quantify the
100 magnitude of variation in erodibility between rock types by: (i) extracting the normalised river
101 channel steepness of rock units from a digital elevation model; (ii) collecting mechanical
102 measurements of rock strength in the field, and (iii) quantifying the mobility of the drainage divide
103 using topographic metrics. Our measures of rock erodibility and stratigraphic orientation are then

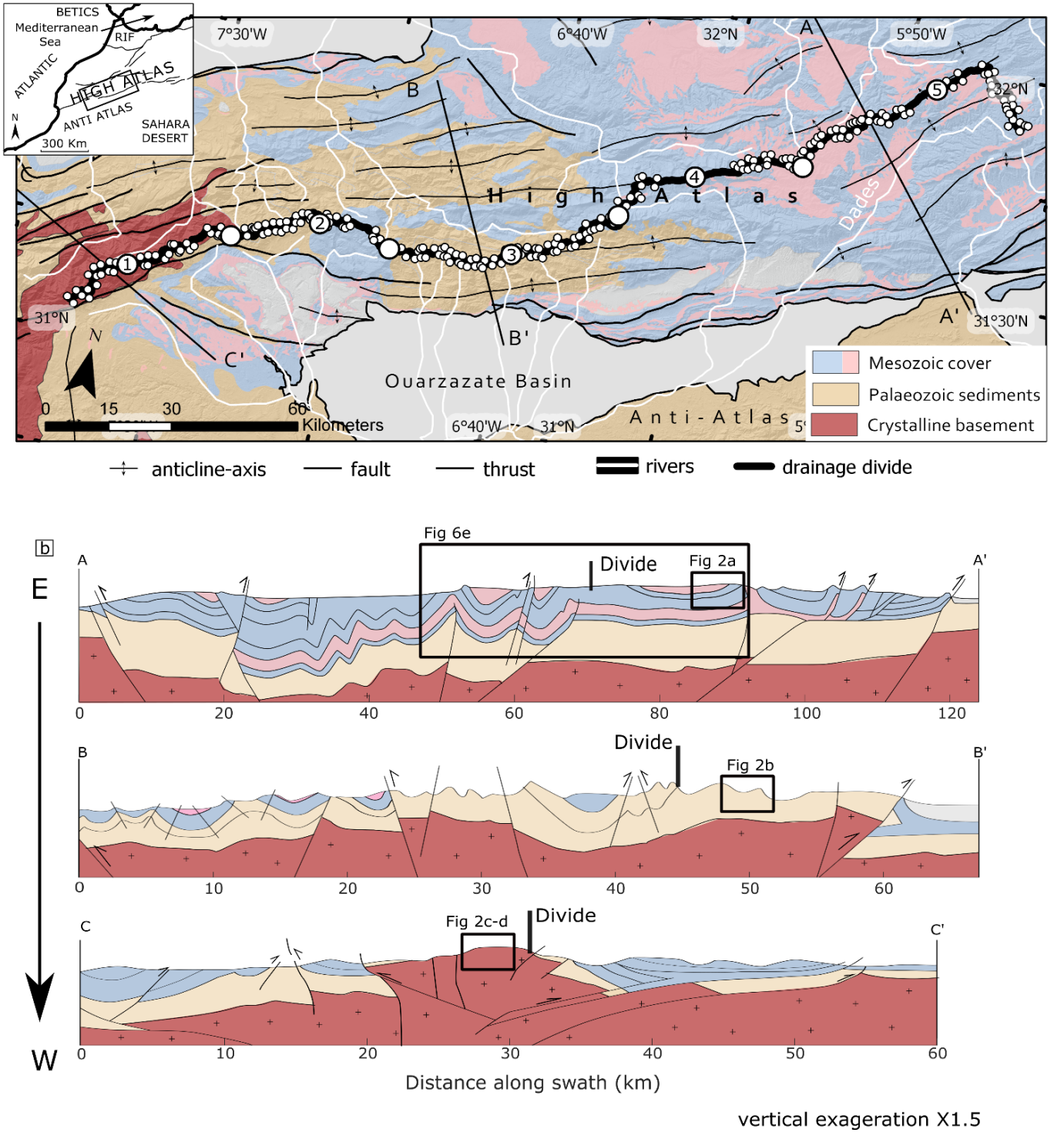

Figure 1 – a) Geological map of the central High Atlas, showing the distribution of Mesozoic sedimentary cover consisting of limestones (blue) and continental clastic sedimentary rocks (pink), Palaeozoic meta-sediments (orange) and crystalline basement (red). The chain is flanked by sedimentary basins: the Ouarzazate Basin to the south and the Haouz Basin to the North. Three cross-sections labelled A to C show the locations of cross-sections in b). Headwater channel locations used for calculating drainage divide mobility start at a reference drainage area of 1 km2, marked as white dots (see methods 3.3). The drainage divide is marked on as a black line and is segmented into five equal lengths (Fig. 5). b) Cross-sections based on seismic sections modified from Errarhaoui (1998); Teixell et al. (2003). These cross-sections are vertically exaggerated by a factor of 1.5. The location of the drainage divide is marked on as black markers on the structural cross sections.

variation in the evolution of a collisional mountain belt in which rivers erode first through sedimentary cover, secondly through meta-sediments and finally through crystalline basement. Results from this study have implications for understanding long-term trends in the geomorphology and erosion of mountain belts owing to the rock types and their structural configuration, and quantitatively constrain the magnitude of contrasts in erodibility within a mountain belt which enables integration of observation and modelling studies.

2 Study area

The study area is located in the centre of the High Atlas Mountains, focussed on the 250-300 km length of the drainage divide bounded by the Ouarzazate Basin to the south and the Haouz Basin in the north (Fig. 1). The drainage divide strikes along the structural grain of the mountain belt, inherited by the configuration of a pre-existing rift (Babault et al., 2012). The age of exposed bedrock and its associated tectonic architecture in the mountain belt increases from east to west in the study area (Fig. 1). The along strike trends allow us to use location as a proxy for time in understanding the mobility of the main drainage divide as river erosion exposes sedimentary cover to metamorphic sedimentary rock, to crystalline basement. The sedimentary cover, older meta-sediments and underlying crystalline basement have distinct lithologies with varying hardness and structural weaknesses owing to the tectonic architecture of the mountain belt (Table 1). Thus, each chronostratigraphic package has its own potential for drainage divide mobility which we investigate in this study.

From east to west the drainage divide crosses first a landscape dominated by gently dipping beds of Mesozoic carbonates and clastic sedimentary rock (Table 1) configured into low-amplitude long-wavelength folds punctuated by spaced-out thrusts (Fig 1, Fig 2a) at an elevation of 2600 to 3000 m. In this length of the divide, the Dades catchment lies to the south and incises into a long-wavelength syncline exhibiting gently dipping strata, whereas directly north of the divide is a concentration of folding and thrust offset strata dipping at higher angles to the surface (Fig. 1b). Next the drainage

Table 1 - chronostratigraphic packages labelled on Fig 1 with details of lithologies and structure

Chronostratigraphic package	Lithologies	Structure	Rock strength (see Table 2 for definitions)
Mesozoic sedimentary cover	massive marine platform limestones; continental red marls with gypsum; marine and continental conglomerates, sandstones, siltstones and micro-conglomerates	horizontal stratigraphy, gently deformed with spaced-out faults and thrust-top folds offsetting strata vertically	very weak – moderately strong
Palaeozoic meta-sediments	sandstones, shales, siltstones, schists	closely spaced faults, abundant jointing, steeply dipping and folded strata	moderately strong
Crystalline basement	granite, granodiorite, gabbro, dolerite, migmatite	massive outcrops of igneous rock, vertical or sheet fracturing in some outcrops	strong

divide decreases in elevation to ~2500 m, as it crosses a zone of dipping strata of faulted meta-sediments (Table 1, Fig. 2b) in the centre of the study area (Fig.1). Finally, in the west, the divide rises back up to elevations > 2800 m as it runs over the edge of the exhumed crystalline basement consisting of igneous rocks with vertical or sub-vertical fracturing (Fig. 1, Table 1, Fig 2c-d).

The inland setting of the central High Atlas (800-1000 km from the coast) results in an absence of eustatic base level control on drainage development. Though localised base level fluctuations are likely to have occurred, studies of basin fill sediments and river profiles suggest that such fluctuations were small to negligible over the Plio-Quaternary (Boulton et al., 2014; Boulton et al., 2019). The High Atlas is in a post-orogenic state, with long-term isostatic rock uplift rates of 0.17-0.22 mm yr^{-1} since 15 Ma related to lithospheric thinning (Babault et al., 2008). The lack of recent

Figure 2 – field photos showing the lithologies and stratigraphic configuration of units within the three lithostratigraphic packages of the Atlas. a) In the Mesozoic weathering-resistant competent limestone beds dip at sub-horizontal angles. Within the interlayered limestones and weaker clastic rocks, variations in rock strength and weathering exist. b) In the Palaeozoic meta-sediments steeply dipping, sub-vertical strata are common. Road on the flood plain for scale. c) Massive crystalline basement exposed in is sometimes found jointed in vertical plains or d) as dome-shaped or massive igneous outcrops with vertical or sheet fracturing. House for scale at the bottom.

tectonic deformation is apparent in the undeformed continuous Quaternary river terraces forming parallel river long profiles throughout the fold-thrust belt and thrust front (Stokes et al., 2017). Therefore, unlike in active mountain belts where divide migration is expected in response to changes in the uplift field (Willett et al., 2001), the Plio-Quaternary divide mobility of the High Atlas is not expected to reflect tectonic advection. Recorded glacial features related to Pleistocene glaciation establish that the snowline was at c. 3300 m in the High Atlas (Hughes et al., 2004). Since the main drainage divide varies in elevation between 2500-3000 m it has not been affected significantly by glacial activity. Thus, for our purposes the main control on the Plio-Quaternary evolution of the High Atlas river network is the incision through the inherited tectonic architecture of lithological units and their contrasting strengths. Drainage development in the High Atlas is considered to be primarily the product of the exhumation of structurally distributed lithologies with different hardness, controlling where river terraces develop (Stokes et al., 2017) and affecting the occurrence of diffusive and

advective slopes (Mather and Stokes, 2018). The High Atlas is set in a semi-arid climate, which means that the effect of weathering on rock erodibility is expected to be low. Thus, intact rock strength measurements are likely to reflect the effective bedrock strength.

3 Methods

We measure two proxies of fluvial bedrock erodibility to constrain the contrast between lithological units. These data allow us to compare our field observations of drainage divide mobility with numerical models of river erosion through variable lithology. We systematically: 1) derive the normalised river channel steepness index from a digital elevation model (DEM) as a measure of a river channel's power to erode rock; 2) record compressive rock strength using a Schmidt hammer in the field as another measure of fluvial erodibility, and 3) extract topographic metrics of drainage divide mobility from the DEM along the length of the main drainage divide.

3.1 River profile analysis, rock type and fluvial erodibility

Rock type influences the river network by affecting the ability of rivers to erode into bedrock, determined by the fluvial erodibility. Numerical models that describe river erosion through bedrock often use the stream power model, in which the erosion rate at any particular point in a bedrock river channel is defined by:

$$E = KA^m S^n \quad \text{(Eq. 1)}$$

where *K* is an erodibility constant which depends on the rock-type over which the river channel flows as well as the climatic setting, *A* is upstream drainage area and *S* is local channel gradient, and *m* and *n* are constants that depend on basin hydrology, channel geometry, and erosion processes (Whipple and Tucker, 1999). Any change in the erodibility of rock type exposed will force the river to adjust its stream power by changing river channel slopes and thus can cause divide mobility as river networks respond. The use of this formula in field studies proves problematic because of the lack of

177 data and robust methodology to determine the erodibility constant, *K*. However, equation 1 can be
178 written as

179 $$S = \left(\frac{E}{K}\right)^{\frac{1}{n}} A^{-(m/n)} \qquad \text{(Eq. 2)}$$

180 which may be recognised as a form of the empirical power law scaling local channel gradient (*S*) and
181 drainage area (*A*):

182 $$S = k_{sn} A^{-\theta} \qquad \text{(Eq. 3)}$$

183 $$k_{sn} = \left(\frac{E}{K}\right)^{\frac{1}{n}}$$

184 $$\theta = m/n$$

185 where *S* is the local channel slope (dimensionless), k_{sn} is normalised steepness index ($m^{2\theta}$) and θ is
186 the concavity index (dimensionless). We assume that erosion is proportional to specific stream
187 power and inversely proportional to bedrock erodibility, so that n > 1 (Perne et al., 2017), and k_{sn} is
188 inversely proportional to erodibility, *K*:

189 $$K \propto \frac{1}{{k_{sn}}^{n}} \qquad \text{(Eq. 4)}$$

190 Unlike *K*, the k_{sn} of river channels can be readily determined from digital elevation models (DEMs)
191 (e.g. Boulton et al., 2014; Gallen, 2018; Bernard et al., 2019). We therefore use k_{sn} as a measure of
192 fluvial erodibility of geological units over which river channels flow in the High Atlas, provided that
193 spatial variability in long term rock uplift is low, which is likely, for reasons outlined above (Section
194 2). Consequently, a factor of difference in k_{sn} between geological units will be an estimate of the
195 factor of difference in their fluvial erodibility, *K*. We normalise k_{sn} values to the most erodible rock-
196 type (see section 4.1), and then use Eq. 4 to convert these normalised average k_{sn} values to
197 normalised *K* values. To do this, we calculate normalised K for three feasible values of n: n=1, n=2
198 and n=4. Perne et al. (2017) show that to obtain a stream-power-model generated river profile in

199 which the slopes of river channels are steeper in low erodibility, strong rock, n must be > 1. Lague
200 (2014) demonstrate that, fully calibrated with slope information from field locations, n ~ 2 in most
201 cases, and this could be as high as n ~ 4. Calculating normalised K values from the k_{sn} data enables a
202 quantification of contrasts in erodibility *K* between rock-types in the High Atlas and their control on
203 changes in river erosion rates and consequent mobility of the drainage divide.

204 We performed k_{sn} analysis using the Topographic Analysis Kit (Forte and Whipple, 2019), a series of
205 MATLAB functions based on TopoToolbox (Schwanghart and Scherler, 2014) which uses the chi
206 approach to calculate k_{sn} smoothed over 1000 m segments (Perron and Royden, 2013). Tests using
207 the criteria proposed by Perron and Royden (2013) show that θ is ~ 0.45 for a range of catchments
208 covering the extent of the drainage divide in the central High Atlas, which is the same value as used
209 for the High Atlas by Boulton et al. (2014). This gives k_{sn} units of $m^{0.9}$. We use the ALOS Digital
210 Elevation Model with a resolution of 30 m from the Japan Aerospace Exploration Agency
211 (http://www.eorc.jaxa.jp/ALOS/en/aw3d30/index.htm) to perform the analysis following
212 recommendations of Boulton and Stokes (2018). Finally, we extract the average and standard
213 deviation k_{sn} of each rock type using the digitised 1: 1 000 000 geological map of Morocco (Saadi et
214 al., 1985, see Supplementary Fig. S1). Formations are grouped into lithological units that collectively
215 comprise three groups: Mesozoic sediments, Palaeozoic meta-sediments and crystalline basement
216 over which the drainage divide crosses from east to west (Fig. 1). For each of those packages we
217 group lithological units (Table 1): (i) gently folded massive marine platform limestone; (ii)
218 interbedded red beds consisting of mud and siltstone; (iii) interbedded sand-siltstones and
219 conglomerates; (iv) folded and faulted meta-sedimentary rocks such as schist and shale, and (v)
220 faulted massive outcrops of igneous units. The contrasts in k_{sn} of river channels flowing over rock-
221 types (Supplementary Fig. S1) includes the effects of both rock strength and structural weaknesses
222 on the resulting erodibility of bedrock.

223

3.2 Mechanical rock strength measurements, rock type and erodibility

A further approach to determine the fluvial erodibility of rock-types is measuring their mechanical strength. The classic experiment by Sklar and Dietrich (2001) showed that erodibility of rock, *K*, in the stream power model for bedrock river erosion is related to the inverse square of tensile strength ($\sigma_\tau{}^2$). Thus, a measure of tensile strength and the difference between units enables the calculation of contrasts in erodibility, *K*. However, measurements of tensile strength cannot be achieved easily in the field, and the most commonly applied method of rock strength assessment in geomorphology is the Schmidt hammer because of its portability (Goudie, 2006). The Schmidt hammer records the rebound distance of a weighted spring that strikes the rock surface and uses a range from 10 – 100. With the Schmidt hammer, measurements of *in situ* uniaxial compressive rock strength in the landscape can be taken in large quantities, making it a very versatile instrument in landscape studies. The higher the rebound value, the higher the elastic strength of the rock, which is a measure of the uniaxial compressive strength (UCS) of a rock. Tensile strength (TS) represents the resistance to sediment impacts on the riverbed and its use has been advocated based on the stronger correlation of fluvial metrics with tensile strength than compressive strength (Bursztyn et al., 2015). But since compressive and tensile strength are correlated (UCS ~ 10*TS; Kahraman et al., 2012; Nazir et al., 2013), *K* is effectively also proportional to the inverse square of UCS: $K \propto \frac{1}{UCS^2}$ (Eq. 5)

Thus, similar to the approach in 3.1, we normalise UCS values to the most erodible rock-type, and then use Eq. 5 to convert these normalised average UCS values to normalised *K* values. To produce a map of rock strength we digitised the 1:1 000 000 geological map of Morocco (Saadi et al., 1985) for the study area and assigned an average rock rebound value to each stratigraphic unit. Typically, ten to twenty Schmidt hammer measurements were taken at each location, totalling 690 readings throughout the central High Atlas with up to 132 readings per geological unit (Supplementary materials). Where rock strength measurements for geological units from field measurements were absent, we supplemented this with an existing database of Schmidt rebound values for lithological

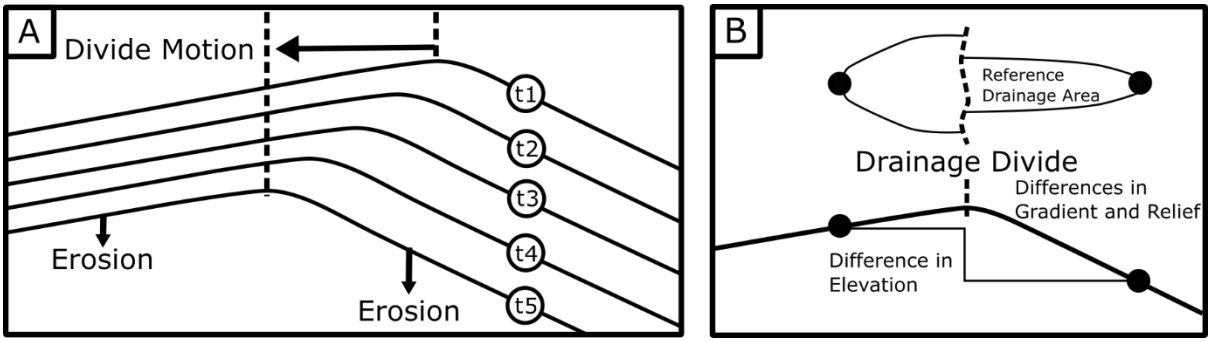

Figure 3 – principles of the Gilbert metrics for drainage divide stability, modified after Forte and Whipple (2018). Where channels are steeper on one side of the divide compared to the other, divide motion will be in the direction of low gradients where erosion is lower. B) Similarly, erosion will progress towards those channels with higher headwater channel elevations.

units reported from around the world (Goudie, 2006). This database contains Schmidt rebound measurements for 111 lithological units, in mostly arid environments similar to the High Atlas. For each stratigraphic unit without field measurements the average of values reported in the literature for the lithology of that unit is used. Units are combined in the same lithological groups as the k_{sn} data. The standard deviation of Schmidt hammer measurements and the range of values reported in the literature reflect the variation of rock strengths within the lithological units (Supplementary material Table 1, Figure S2). Mean and standard deviation of Schmidt hammer rebound values (SHV) are then converted to UCS using the conversion which was derived by Katz et al. (2000) ($UCS = 2.21e^{(0.07SHV)}$) for a range of carbonate rocks, sandstone, marble and igneous rocks with UCS values similar to those found in the study area. In contrast to the k_{sn} approach, the UCS of lithological units only takes into account the internal rock mass strength of bedrock, and thus does not account for structural weaknesses imposed by discontinuities such as bedding or jointing. Consequently, estimating variation in erodibility between rock-types using this approach may be expected to underestimate the erodibility of folded and faulted shales and schists and jointed igneous rock (Table 1).

3.3 Topographic analysis of the drainage divide

To determine the mobility of the drainage divide in response to erodibility variation and its structural configuration, we perform topographic analysis of the main drainage divide along the

study length. The mobility and potential direction of movement of the drainage divide depends on erosion rates either side, and whilst the chi method of mapping drainage divide instabilities (Willett et al., 2014) is used widely, Forte and Whipple (2018) demonstrated that this method is especially problematic when integrating across multiple lithologies with different strengths. Alternatively, Forte and Whipple (2018) coined the term Gilbert Metrics, based on the assumption that contrasting stream gradients either side of a divide will drive divide migration. Where divides are bounded by different channel gradients either side they are mobile, with higher erosion rates on the steeper sides leading to migration towards the side with lower channel gradients (Fig. 3). The topographic proxies for erosion rates across divides defined by Forte and Whipple (2018) are differences in headwater channel elevation, local headwater hillslope gradient and local headwater relief, which have proven useful for interpreting the relative mobility of catchment divides (Forte and Whipple, 2018). Headwater channel elevation, local headwater hillslope gradient and local headwater relief were extracted from the ALOS DEM using methods outlined in Forte and Whipple (2018), at a reference drainage area 1 km^2. While the upstream area required to initiate channel flow varies on settings (Clubb et al., 2014), this drainage area is the critical threshold area downstream of which stream-flow-dominated fluvial channels are expected to dominate over debris-flow-dominated colluvial channels in most settings (Wobus et al., 2006). In a numerical landscape evolution model, Forte and Whipple (2018) test the applicability of the Gilbert metrics in a setting with erodibility contrasts across a drainage divide, and conclude that divide migration rate approximates a linear relationship with cross-divide differences in erosion rates and all three Gilbert metrics. To assess the mobility of the drainage divide we define five equal lengths of about 50 km each where boundaries align with those of the three lithological packages described earlier (Fig. 1), and in each the mean, standard deviation, standard error and bootstrap confidence interval of headwater channel values are calculated either side of the drainage divide.

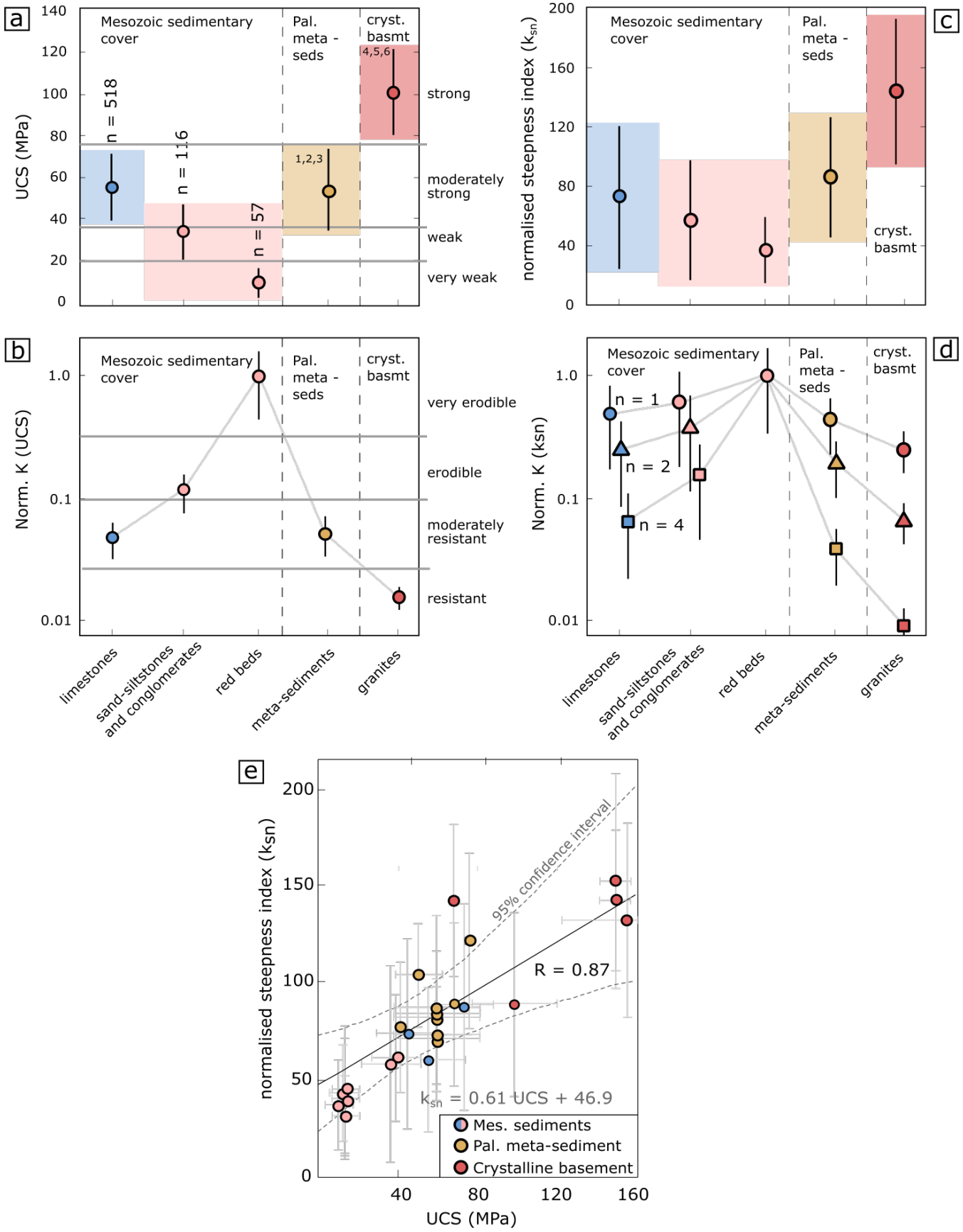

Figure 4 – Average and standard deviation of a) uniaxial compressive strength b) k_{sn} for every chronolithological unit. The number of values analysed for each lithology is displayed above the plots. Colours in graphs are in accordance with Fig. 1. Sources of compressive strength data: 1) Gokceoglu and Aksoy (2000) 2) Goudie (2006) and references cited therein 3) Goktan and Gunes (2005) 4) Karakus et al. (2005) 5) Pye et al. (1986) 6) Kahraman et al. (2002). Fluvial erodibility K for each chronolithological unit normalised against the weakest rock type derived from relative UCS values (c) and relative k_{sn} values (d). In d), values of normalised K derived from ksn depend on the value of variable n in the stream power equation (Eq. 4) e) Linear regression of values of k_{sn} and UCS for every geological unit (geological map 1:100 000) with a 95 % confidence envelope in dashed grey lines and points coloured by chronolithological membership. R is the correlation coefficient. Classification of rock strength is based on Schmidt hammer values and other measures of rock strength summarised in Table 2, modified from Goudie (2006). Erodibility classification is based on rock strength (Table 2).

Table 2 – Classification of rock-type, strength and fluvial erodibility

Description	**Schmidt hammer value**	**Uniaxial compressive strength**	**Characteristic rocks**	**Fluvial erodibility**
Very weak rock – crumbles under sharp blows with geological pick point, can be cut with pocket knife	10-30	1-20	Weathered and weakly compacted sedimentary rocks – rock salt, marls	Very erodible
Weak rock – shallow cuts or scraping with pocket knife with difficulty, pick point indents deeply with firm blow	30-40	20-35	Weakly cemented sedimentary rocks – siltstones and conglomerates	Erodible
Moderately strong rock – knife cannot be used to scrape or peel surface, shallow indentation under firm blow from pick point	40-50	35-75	Competent sedimentary rocks – limestone, dolomite, sandstone, shale, slate, schist	Moderately resistant
Strong rock – hand-held sample breaks with one firm blow from hammer end of geological pick	> 50	> 75	Competent igneous and metamorphic rocks – granite, migmatite, granodiorite, basalt	Resistant

Rock strength classification and descriptions modified from Table 2 in Goudie (2006)

4 Results

In plan view (Fig 1a), the drainage divide follows a sinuous form, with lengths mostly configured to ENE-WSW and WNW-ESE orientations. The divide tends to occupy central positions in relation to the topography of the range apart from a notable southerly segment in the middle of the study area. Only in the eastern end is there a marked deviation in divide orientation where a small length (20 km) changes to NW-SE.

With respect to erodibility, the drainage divide from east to west runs over bedrock of differing erodibilities, quantified through k_{sn} and UCS measurements.

304 *4.1 K_{sn} and fluvial erodibility*

305 From east to west, the drainage divide runs over moderately resistant to erodible and very erodible
306 sedimentary cover, moderately resistant meta-sediments, and resistant crystalline basement (Fig. 1).
307 Red beds, other clastic sediments and limestones in the Mesozoic cover have mean k_{sn} values of 37,
308 59 and 74 $m^{0.9}$ with standard deviations of 25, 42 and 49 $m^{0.9}$ respectively (Fig. 4c). Palaeozoic meta-
309 sediments average at 85 $m^{0.9}$ with a standard deviation of 41 $m^{0.9}$, whilst the crystalline basement
310 has the highest k_{sn} at 146 with a standard deviation of 52 $m^{0.9}$ (Fig. 4c). Fluvial erodibility *K* values
311 based on Eq. 4 and k_{sn}, normalised to the Mesozoic red beds (the weakest lithology: section 3.2),
312 vary by a factor of four to fifteen (Fig. 4d). The normalised *K* value for red beds is 1.0, with other
313 clastics 0.40 or 0.63 and limestone in the Mesozoic cover at 0.25 or 0.50, depending whether n = 2
314 or n = 1 (Fig. 4d). Normalised *K* for Palaeozoic meta-sediments is 0.19 or 0.44 whilst crystalline
315 basement has the lowest normalised *K* at 0.066 or 0.26, about four to fifteen times less erodible
316 than the Mesozoic red beds.

317 *4.1 UCS and fluvial erodibility*

318 Similar to the k_{sn} of rock units, the fluvial erodibility of bedrock along the length of the drainage
319 divide based on UCS varies from alternating very erodible to moderately resistant rock in the
320 sedimentary cover, to moderately resistant in the meta-sediments and resistant in the crystalline
321 basement. The Mesozoic sedimentary cover has the largest range in UCS of the three
322 chronostratigraphic packages, with red beds, other clastic sediments and limestones averaging 12,
323 36 and 57 MPa respectively, with standard deviations of 7, 12 and 18 MPa (Fig. 4a). UCS values for
324 the Palaeozoic meta-sediment averages at 55 MPa with a standard deviation of 19 MPa, similar to
325 the Mesozoic limestones (Fig. 4a). The igneous rocks of the crystalline basement have the highest
326 UCS values with a mean and standard deviation of 101 and 20 MPa. Grouping of rocks into five
327 classes is based on a table from Goudie (2006) which is based on Schmidt hammer values and other
328 measures of rock strength (Table 2), and classes are marked on the UCS graph (Fig. 4a). Fluvial

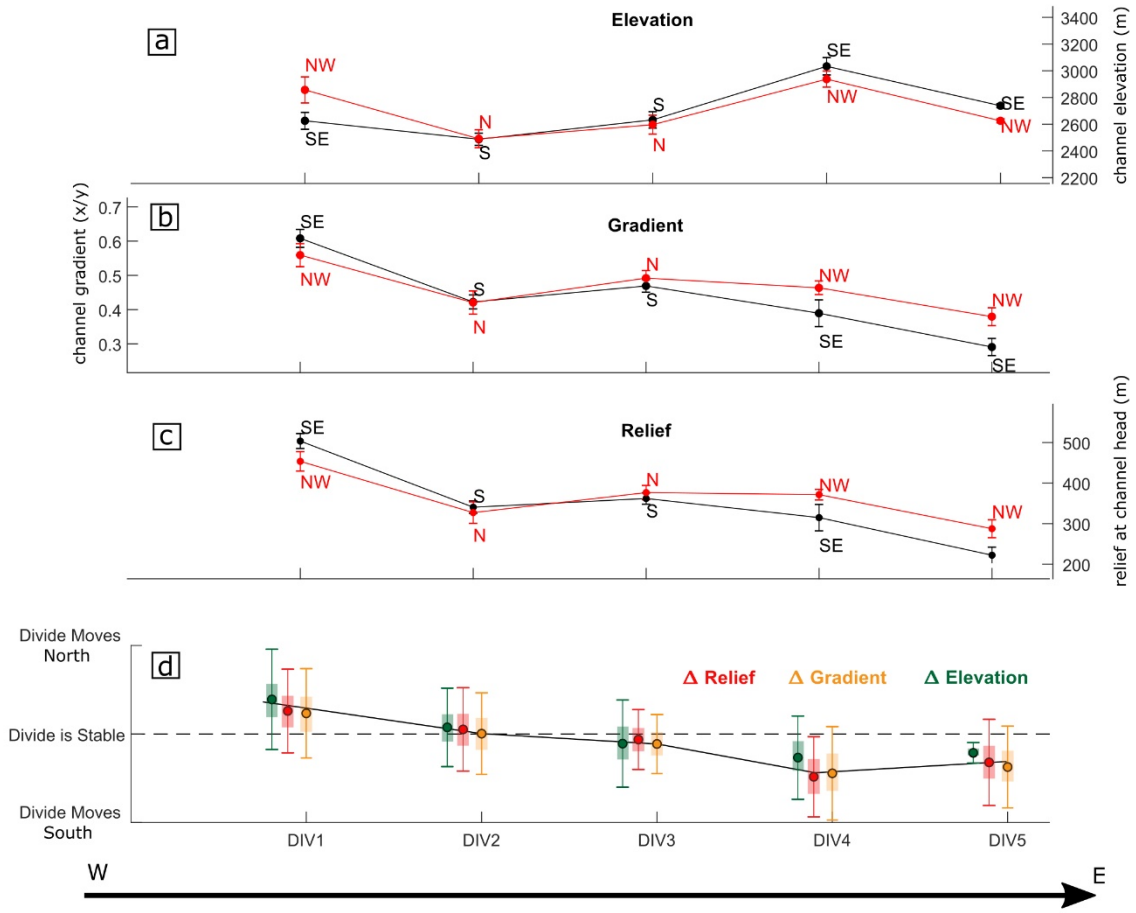

329

Figure 5 – Gilbert metrics for each length of the drainage divide (Fig. 1) from west to east. a-c) headwater channel mean and standard error elevation, gradient and relief respectively. d) Potential direction of divide migration indicated by the direction of mobility of the divide from the Gilbert metrics. Values are standardized to show the direction of mobility. Bars show the standard deviation and shaded boxes show bootstrap confidence intervals.

330 erodibility *K* values based on Eq. 5 and UCS, normalised to the weakest unit, vary by two orders of
331 magnitude (Fig. 4b). The normalised *K* value for red beds is 1.0, with other clastic and limestone in
332 the Mesozoic cover at 0.1 and 0.05 respectively. Normalised *K* for Palaeozoic meta-sediments is 0.05
333 whilst crystalline basement has the lowest normalised *K* at 0.015, about two orders of magnitude
334 less erodible than the Mesozoic red beds. Categories of erodibility suggested based on the
335 lithological grouping into rock strengths (Table 2) and their respective normalised *K* values based on
336 UCS are defined in Fig. 4b.

337 *4.2 Drainage divide mobility*

338 Normalised cross-divide delta values of the Gilbert metrics following Forte and Whipple (2018) show
339 the magnitude and direction of mobility varies along the divide and that the divide is stable in the

340 central length of the divide (Fig. 5). Elevation of the drainage divide is high in both the east and west,
341 around 2600-3000 m in DIV 1 and DIV 4-5, and lowest in the middle length at ~ 2500 m (Fig. 5a). This
342 low elevation length (DIV 2-3) of the divide in the centre of the study area has equal headwater
343 hillslope gradients and relief on both sides of the divide (Fig. 5b-c) suggesting a stable drainage
344 divide in the meta-sedimentary rocks (Fig. 1, 5d). From west to east, headwater hillslope gradients
345 and relief decrease from 0.6 (35°) and 500 m in the crystalline basement of DIV 1 to 0.3 (15°) and
346 220 m in the Mesozoic sedimentary cover of DIV 5. Values of headwater channel elevation, hillslope
347 gradient and relief differ either side of the drainage divide in the eastern (DIV 1) and western (DIV 4-
348 5) lengths (Fig 5b-c). In DIV 1, the Gilbert metrics indicate northward movement of the divide (Fig.
349 5d) towards the centre of the exposed crystalline basement. This mobility is based on headwater
350 values which are on average 169 m higher in elevation to the north, with lower hillslope gradients
351 and relief, which differ by 0.06 (3.4°) and 50 m of relief (10%) across the divide (Fig. 5a-c). In DIV 4
352 and 5 in the Mesozoic cover the divide is significantly mobile towards the south (Fig. 5d), with
353 headwater channel elevation contrasts of 96-113 m, a difference in hillslope gradients of 0.07-0.09
354 (4-5°) and relief 44-55 m (14-30%) (Fig. 5a-c).

355 **5 Discussion**

356 *5.1 Rock strength, k_{sn} and fluvial erodibility*

357 The theory and empirical relationships outlined in sections 3.1 - 3.2 predict that fluvial erodibility, *K*
358 relates to UCS in an inverse square (Eq. 5) and to k_{sn} in an inverse relationship in which the power
359 depends on the value of n (Eq. 4). We find a linear relationship between UCS and k_{sn}, which suggests
360 that n = 2, such that k_{sn} and UCS scale according to a linear relationship. However, visual inspection
361 of figures 4c and 4d suggests that normalised *K* values calculated from k_{sn} data where we assume n =
362 4 are more similar to the normalised *K* values derived from UCS data. However, since Lague (2014)
363 found that n ~ 2 is most commonly observed in the field, and our regression of UCS and k_{sn} data
364 yields a strong linear fit consistent with n = 2, we suggest that n ~ 2 and that any difference between

365 UCS and k_{sn}-derived normalised *K* values is due to other effects. For example, UCS does not explicitly
366 include other factors influencing bedrock erodibility including the degree of weathering and
367 structural discontinuities (Table 1), which especially through zones of deformation, will lead to more
368 rapid erosion of even hard rocks (high UCS) by fluvial systems. For example, Anton et al. (2015) and
369 Baynes et al. (2015) showed that canyons can be created by extreme flood events in basalt and
370 granite respectively, where the presence of discontinuities enables rapid erosion through fluvial
371 plucking and block topple. On the other hand, whilst the stream power model of bedrock river
372 erosion only accounts for changes in river channel slope, field studies show that rock strength
373 correlates with channel width (Allen et al., 2013), as well as valley width (Schanz and Montgomery,
374 2016) and can influence the efficiency of river bed load in eroding underlying bedrock (Brocard and
375 van der Beek, 2006). Furthermore, there can be a dampening of k_{sn} value variations across
376 lithological boundaries as sections of river with weak bedrock downstream of river reaches with hard
377 bedrock can be armoured with blocks (e.g. Thaler and Covington, 2016). Based on the lithological
378 effects on river channel and valley morphology demonstrated by these field studies, using k_{sn} as a
379 measure of rock erodibility in the stream power model of bedrock river incision likely
380 underestimates the effect of lithology on river erosion.

381 Thus, calculated through UCS measurements, *K* is expected to vary by two orders of magnitude (Fig.
382 4c), whereas if using k_{sn}, *K* is expected to vary by one order of magnitude only (Fig. 4d). The lack of
383 constraints of *K* in natural settings have led to numerical modelling studies varying widely in the
384 range of erodibilities, using from one (Forte et al., 2016), two (Yanites et al., 2017), to three orders of
385 magnitude difference between rock-types (Roy et al., 2015). Such a range of inputs is often based on
386 the experimental relationship between intact rock strength and erosion in the classic abrasion mill
387 experiment done by Sklar and Dietrich (2001), and the five orders of magnitude difference in *K*
388 derived through the early work of Stock and Montgomery (1999). The latter forward-modelled river
389 paleo-profiles, constrained by bedrock strath terraces and basaltic layers, to presently observed
390 profiles for a range of locations worldwide. Their values of *K* range from 10^{-2} to 10^{-4} $m^{0.2}$ yr^{-1} in the

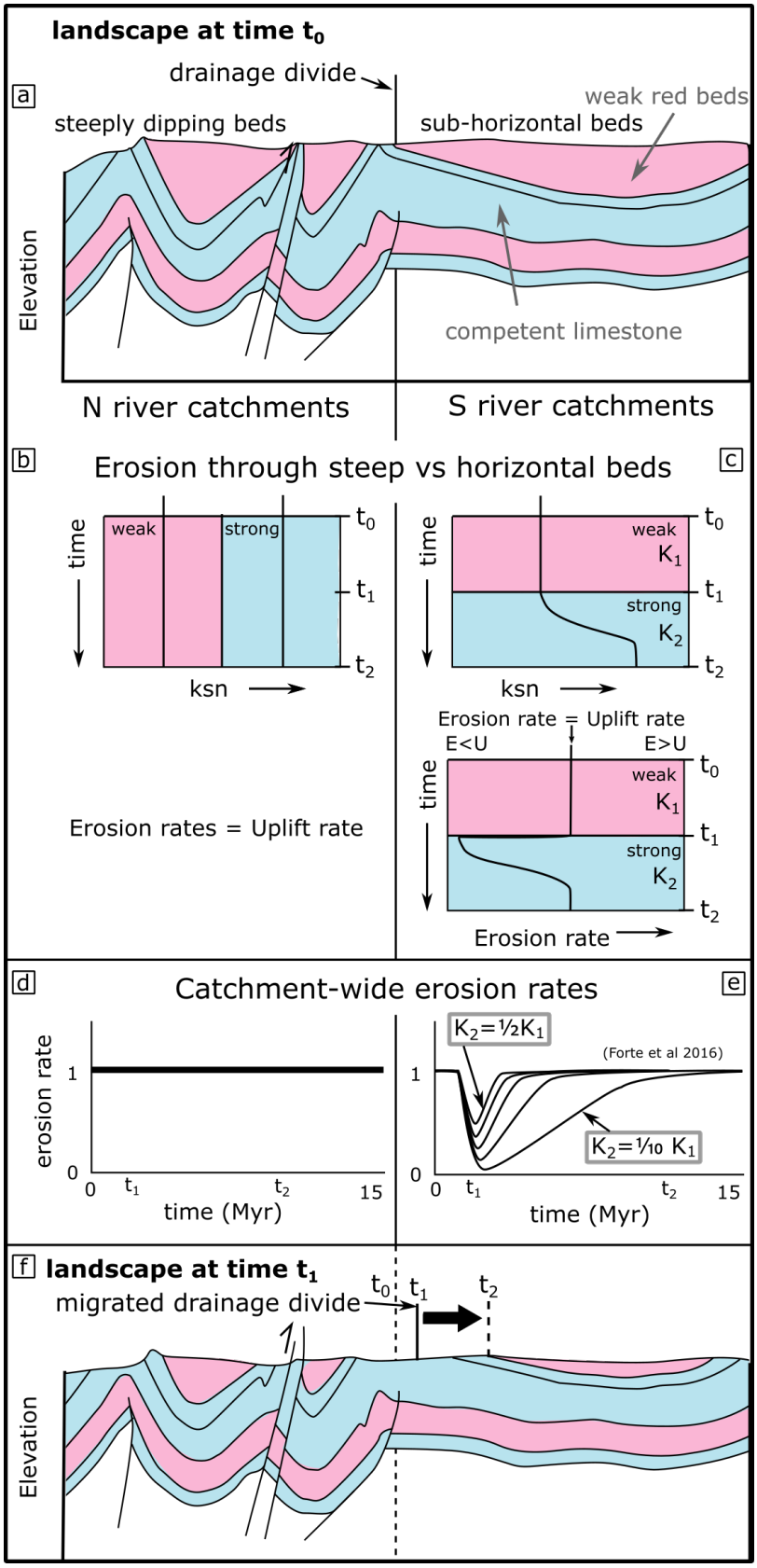
landscape at time t_0
a
drainage divide
steeply dipping beds
sub-horizontal beds
weak red beds
Elevation
competent limestone
N river catchments
S river catchments
b
Erosion through steep vs horizontal beds
c
time
weak
strong
t_0
t_1
t_2
ksn
K_1
K_2
Erosion rate = Uplift rate
E<U
E>U
Erosion rates = Uplift rate
Erosion rate
d
Catchment-wide erosion rates
e
erosion rate
1
0
time (Myr)
15
$K_2=½K_1$
(Forte et al 2016)
$K_2=⅒ K_1$
f
landscape at time t_1
migrated drainage divide

Figure 6: The erosion and exposure of a hard limestone layer underneath a soft red bed layer in the Mesozoic low amplitude syncline leads to a divide mobility towards the southern catchment (Fig. 5). Panel a) shows the landscape at time t_0 with the location of the divide between southern catchments with underlying sub-horizontal strata and northerly catchments with steeply dipping strata. b,c) As the rivers erode through the sub-horizontal strata of the southern catchment the k_{sn} of the surface exposed needs to adjust to the new lithological strength, steepening transiently as it incises into harder limestone bedrock. During the response, erosion rates in the catchment drop before re-establishing equilibrium with uplift rates. On the other hand the northerly catchments do not experience such a change in k_{sn} and experience steady rates. d,e) Graphs show the change in catchment-wide erosion rates either side of the drainage divide from t_0 to t_1 when the lithological contact gets exposed in the southern catchment to time t_2 when erosion rates have reached steady state. The graph for the southern catchments shows the results from landscape evolution modelling of the exposure of a contact between sub-horizontal soft stratigraphy on top of a hard layer (Forte et al., 2016). The resultant change in erosion rates across the divide explains the migration of the drainage divide. The response depends on the factor of difference in erodibility, K, between units. Panel f) shows how the erosion of the lithological contact in the southern catchments leads to drainage divide migration to the south over the time of the transient response.

mudstones of humid continental Japan, to 10^{-6} - 10^{-7} $m^{0.2}$ yr^{-1} in the subtropical granite landscape of Australia (Stock and Montgomery, 1999). An issue with the experimental approach by Sklar and Dietrich (2001) is that it does not include the effects of weathering and jointing of rock in natural landscapes and their influence on fluvial erodibility. In the results from Stock and Montgomery (1999) the influence of rock-type is difficult to isolate from the variation in climatic setting owing to the spread of study locations. Thus, whilst these early studies give some first order estimates of possible absolute values of fluvial erodibility and the relationship between rock strength and erosion rates, our results constrain more fully the contrasts in fluvial erodibility between rock types which may be expected within a mountain belt.

Next to rock strength control on k_{sn}, orographic enhancement of precipitation with greater precipitation on the northern and western sides of the drainage divide may lead to in a decrease of k_{sn} values from south to north or east to west (Supplementary Fig. S3). However, there is no evidence to suggest a significant difference in k_{sn} values between north and southern or east and western portions of the High Atlas (Supplementary Fig. S4).

5.2 Drainage reorganisation in sedimentary cover

The Gilbert metrics indicate drainage divide mobility where it crosses the sedimentary cover in the east (Fig. 5d). Here, the Mesozoic sedimentary cover is gently deformed, resulting in gently dipping strata punctuated by widely spaced thrusts and folds (Fig 1b, Fig 2a). For example, the Dades river catchment south of the main drainage divide (Fig. 6a) incises into a long-wavelength syncline of

411 slightly dipping strata composed of weak continental red beds and hard limestones, whereas directly
412 north of the divide folding and thrusting is more closely spaced resulting in strata dipping at higher
413 angles to the surface (Fig. 6a). Our results show that k_{sn} is correlated to rock strength (Fig. 4e), and in
414 the hard limestone k_{sn} is higher than in the weak red beds (Fig. 4a,c). Whereas erosion through near-
415 vertical strata north of the divide result in near-stable k_{sn} values through time (Fig. 6b), the
416 horizontal stratigraphy of the Dades river catchment to the south of the divide means k_{sn} values
417 need to change through time to return to stable erosion rates (Fig. 6c) which equal rock uplift rates.
418 Consequently, there is a period of transience when k_{sn} values adjust to the change in bedrock
419 erodibility that occurred when erosion of soft red beds exposed hard limestone along the majority of
420 the river catchment (Fig. 1a, 6f). This transition period explains the southwards movement of the
421 divide (Fig. 5d), as erosion rates stay more or less stable in the north (Fig. 6d) whilst transient k_{sn}
422 values cause a temporary decrease in erosion rates in the southern river catchments (Fig. 6e). The
423 stratigraphic effect on river erosion rates presented in Fig. 6e was first demonstrated in a numerical
424 modelling study of river erosion through layered stratigraphy by Forte et al. (2016), who show that
425 for strata of variable erodibility dipping 5° or less the overall erosion rate of the landscape is
426 expected to change by several factors during incision. Here, we show that such an effect can lead to
427 migration of the drainage divide in the gently deformed sedimentary cover in collisional mountain
428 settings (Fig. 6f), where exhumation of hard and soft strata is isolated or offset by faults.

429 Simulations by Forte et al. (2016) show the exhumation of a stratigraphic contact with a factor of
430 two to ten difference in erodibility (Fig. 6e) could take 2 - 9 Ma to re-equilibrate in an area of 800
431 km^2 with a relatively high amount of precipitation (1 m yr^{-1}). Therefore, drainage divide migration in
432 response to the incision through soft red beds to hard limestones in the upper half of the 1500 km^2
433 Dades catchment, representing a change in erodibility by a factor of 2 - 20 (Fig. 4), where rainfall is
434 on the order of 0.1 - 0.5 m yr^{-1}, is expected to persist on a timescale of 10^6 – 10^7 yrs.

435

436 *5.3 Divide migration driven by crystalline basement exhumation*

437 Where crystalline basement is exposed we find the position of the drainage divide is shifting towards
438 the centre of this exposed resistant rock in the High Atlas (Fig. 5). In a numerical simulation,
439 Giachetta et al. (2014) found that when they imposed an erodibility gradient across a drainage
440 divide, which is representative of the exhumation of a crystalline basement such as in the High Atlas,
441 the drainage divide responded by moving towards the side of lower erodibility over a timescale on
442 the order of 10^6 yrs. Bonnet (2009) proposed that such a shift of the drainage divide is accompanied
443 by a split of catchments, creating more and smaller catchments on the side of lower erodibility.
444 Giachetta et al. (2014) also show that on the other side, a growth of larger catchments occurs.
445 Similarly, Bernard et al. (2019) found that the drainage divide in the Pyrenees follows the position of
446 strong plutons. This implies that our results show a transient stage of drainage divide migration in
447 response to exhumation of crystalline basement, where today's drainage divide at the edge of the
448 crystalline basement is expected to be stable in the centre of the strong crystalline basement, or
449 might even continue reorganising within the basement to follow the exhumation of resistant
450 plutons. Giachetta et al. (2014) used two orders of magnitude difference in erodibility values to
451 model this effect, and here we show divide mobility can be driven by exhumation of basement that
452 is only a factor of two less erodible than the overlying meta-sedimentary rock if calculated through
453 k_{sn} (Fig. 4d), and a factor of three less erodible if calculated through UCS (Fig. 4b).

454

455 *5.4 Lithologically induced drainage divide mobility during the long term erosion of a collisional*
456 *mountain belt*

457 The combination of estimations of contrasts in fluvial erodibility of rock types (Fig. 4), geomorphic
458 indicators of drainage mobility (Fig. 5), and considerations of their structural configuration in the

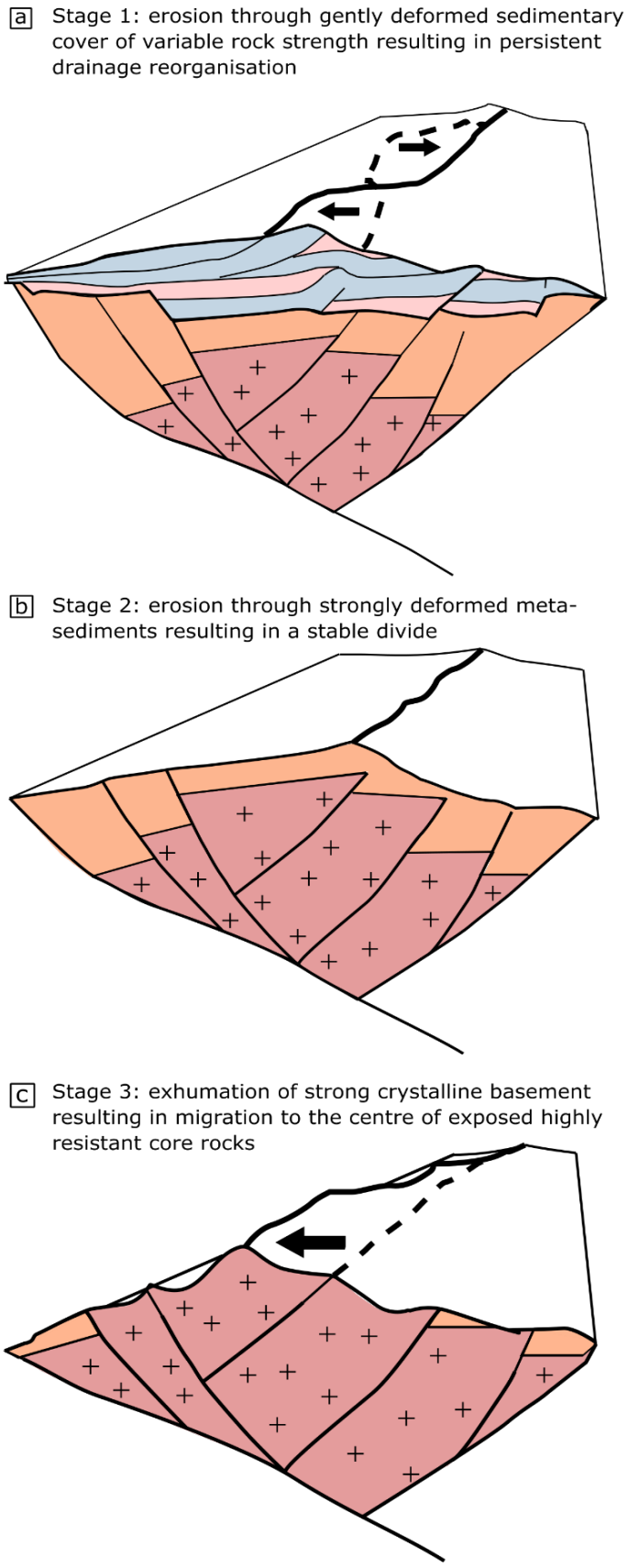

Figure 7 –Conceptual model of the development of a collisional mountain belt and the behaviour of the central drainage divide in response to exhumation of lithostratigraphic units

460 High Atlas compared to numerical simulation studies (see sections 5.1 - 5.3) enables us to propose a
461 model of lithologically-induced drainage divide mobility during the erosion of a mountain belt. The
462 overall trend of the drainage divide, strike of faults and bedding planes follows the structural grain of
463 the mountain belt (Fig. 1), for example determined by the pre-existing structure of an extensional
464 rift such as in the High Atlas (Babault et al., 2012). We purport that changes in erosion rates as rivers
465 incise through strata of different erodibility will drive drainage reorganisation in collisional mountain
466 belts, where layers are close to horizontal and only gently deformed (Fig. 6, 7). This is because where
467 strata are deformed gently and offset by faults, local exhumation of contacts between soft and hard
468 rock leads to changes in erosion rates between catchments (Fig. 6). Consequent changes in erosion
469 rates across the drainage divide will lead to the migration of the drainage divide (Fig. 7a) as
470 illustrated by the mobility of the drainage divide in the High Atlas (Fig 5, 6), which could lead to
471 steady divide migration or instantaneous capture of catchments, such as shown in the Appalachians
472 (Gallen, 2018). The effect of rock type on drainage reorganisation will be strongest in early phases of
473 collisional mountain building, before the sedimentary cover erodes in the centre of the belt. In later
474 stages, minor reorganisation and capture could still occur closer to the thrust front on the margins of
475 the mountain belt where Mesozoic sedimentary strata are present. When deformed meta-sediments
476 become exhumed, the increase in dip and deformation of strata leads to more stable erosion as
477 rivers incise (Forte et al., 2016, Fig. 6), resulting in stable drainage divides as witnessed in the middle
478 of the study area (Fig 5, 7b). When crystalline basement gets exhumed, the drainage divide will
479 migrate into the centre of highly resistant rocks resulting in more drainage divide migration (Fig 5,
480 7c). The migration of the main drainage divide in a mountain belt has been shown to lead to
481 reorganisation of river catchments (Bonnet, 2009; Giachetta et al., 2014), imposing new boundary
482 conditions on river channels which change gradients and sediment loads (Forte et al., 2015) and the
483 ensuing response can result in a cascading effect, impacting geomorphic and stratigraphic systems
484 for millions to tens of millions of years (Beeson et al., 2017). The effects of lithologically-induced

drainage migration here described for a post-orogenic belt could be more complex in an active mountain belt setting.

Conclusions

This study shows that in a collisional mountain belt, the drainage divide will be mobile in response to changes in erosion rates of rivers incising into gently dipping and deformed strata of contrasting erodibility in the sedimentary cover, and in response to the exhumation of strong crystalline basement. A combination of rock mass strength measurements and k_{sn} derived from a digital elevation model constrain the contrasts in fluvial erodibility exhibited in the High Atlas to between a factor of 4 calculated through k_{sn} and two orders of magnitude calculated through UCS. In the stage of a collisional mountain belt during which rivers incise through highly deformed meta-sedimentary units of intermediate erodibility, rock-type induced boundary conditions affect river networks the least. Based on our values of erodibility contrast and previous numerical models we estimate the timescale of adjustment in response to changes in erodibility of exposed bedrock to be on the order of 10^6-10^7 yrs. Our results demonstrate that the mobility of the drainage divide in a collisional mountain belt can be driven by rock erodibility variation alone, which has implications for the perception of autogenic dynamism of drainage networks and fluvial erosion in collisional mountain belts, and the interpretation of their geomorphology and downstream stratigraphy.

Author contributions

J.R.Z. drafted the article with critical revision and intellectual input from co-authors according to the following contribution: M.S., S.J.B., M.T., A.E.M.. J.R.Z., M.S., A.E.M. and S.J.B. performed the Schmidt hammer measurements in the field, J.R.Z. performed the topographic analysis. J.R.Z., M.S. and S.J.B. initiated the project.

Funding

Fieldwork to validate topographic analysis and take Schmidt hammer measurements during J.R.Z.'s PhD was supported by a University of Plymouth PhD studentship and the Geological Remote Sensing Group Student Award.

Acknowledgements

We thank Hugh Sinclair and Adam Forte for constructive comments which allowed us to improve the paper quality. We thank Jean-Philippe Avouac for editorial guidance.

References cited

Allen, G.H., Barnes, J.B., Pavelsky, T.M., Kirby, E., 2013. Lithologic and tectonic controls on bedrock channel form at the northwest Himalayan front. Journal of Geophysical Research: Earth Surface 118, 1806-1825. doi:10.1002/jgrf.20113

Anton, L., Mather, A.E., Stokes, M., Munoz-Martin, A., De Vicente, G., 2015. Exceptional river gorge formation from unexceptional floods. Nat Commun 6, 7963. doi:10.1038/ncomms8963

Babault, J., Teixell, A., Arboleya, M.L., Charroud, M., 2008. A Late Cenozoic age for long-wavelength surface uplift of the Atlas Mountains of Morocco. Terra Nova 20, 102-107. doi:10.1111/j.1365-3121.2008.00794.x

Babault, J., Van Den Driessche, J., Teixell, A., 2012. Longitudinal to transverse drainage network evolution in the High Atlas (Morocco): The role of tectonics. Tectonics 31, n/a-n/a. doi:10.1029/2011tc003015

Baynes, E.R., Attal, M., Niedermann, S., Kirstein, L.A., Dugmore, A.J., Naylor, M., 2015. Erosion during extreme flood events dominates Holocene canyon evolution in northeast Iceland. Proc Natl Acad Sci U S A 112, 2355-2360. doi:10.1073/pnas.1415443112

Beeson, H.W., McCoy, S.W., Keen-Zebert, A., 2017. Geometric disequilibrium of river basins produces long-lived transient landscapes. Earth and Planetary Science Letters 475, 34-43. doi:10.1016/j.epsl.2017.07.010

Bernard, T., Sinclair, H.D., Gailleton, B., Mudd, S.M., Ford, M., 2019. Lithological control on the post-orogenic topography and erosion history of the Pyrenees. Earth and Planetary Science Letters 518, 53-66. doi:10.1016/j.epsl.2019.04.034

Bonnet, S., 2009. Shrinking and splitting of drainage basins in orogenic landscapes from the migration of the main drainage divide. Nature Geoscience 2, 766. doi:10.1038/ngeo666

Boulton, S.J., Stokes, M., 2018. Which DEM is best for analyzing fluvial landscape development in mountainous terrains? Geomorphology 310, 168-187. doi:10.1016/j.geomorph.2018.03.002

Boulton, S.J., Stokes, M., Mather, A.E., 2014. Transient fluvial incision as an indicator of active faulting and Plio-Quaternary uplift of the Moroccan High Atlas. Tectonophysics 633, 16-33. doi:10.1016/j.tecto.2014.06.032

Boulton, S.J., VanDeVelde, J.H., Grimes, S.T., 2019. Palaeoenvironmental and tectonic significance of Miocene lacustrine and palustrine carbonates (Aït Kandoula Formation) in the Ouarzazate Foreland Basin, Morocco. Sedimentary Geology 383, 195-215. doi:10.1016/j.sedgeo.2019.01.009

Brocard, G.Y., van der Beek, P.A., 2006. Influence of incision rate, rock strength, and bedload supply on bedrock river gradients and valley-flat widths: field-based evidence and calibrations from western

549 Alpine rivers (southeast France). In: Tectonics, Climate, and Landscape Evolution, vol.398, pp.101–
550 126. doi:10.1130/2006.2398(07)
551 Bursztyn, N., Pederson, J.L., Tressler, C., Mackley, R.D., Mitchell, K.J., 2015. Rock strength along a
552 fluvial transect of the Colorado Plateau – quantifying a fundamental control on geomorphology.
553 Earth and Planetary Science Letters 429, 90-100. doi:10.1016/j.epsl.2015.07.042
554 Clubb, F. J., Mudd, S. M., Milodowski, D. T., Hurst, M. D., Slater, L. J., 2014. Objective extraction of
555 channel heads from high-resolution topographic data. Water Resour. Res. 50, 4283– 4304.
556 doi:10.1002/2013WR015167.
557 Errarhaoui, K., 1998. Structure du haut-atlas : plis et chevauchements du socle et de couverture
558 (interpretations des donnees geophysiques et geologiques), p. 326 P.
559 Forte, A.M., Whipple, K.X., 2018. Criteria and tools for determining drainage divide stability. Earth
560 and Planetary Science Letters 493, 102-117. doi:10.1016/j.epsl.2018.04.026
561 Forte, A.M., Whipple, K.X., 2019. Short communication: The Topographic Analysis Kit (TAK) for
562 TopoToolbox. Earth Surf. Dynam. 7, 87-95. doi:10.5194/esurf-7-87-2019
563 Forte, A.M., Whipple, K.X., Cowgill, E., 2015. Drainage network reveals patterns and history of active
564 deformation in the eastern Greater Caucasus. Geosphere 11, 1343-1364. doi:10.1130/ges01121.1
565 Forte, A.M., Yanites, B.J., Whipple, K.X., 2016. Complexities of landscape evolution during incision
566 through layered stratigraphy with contrasts in rock strength. Earth Surface Processes and Landforms
567 41, 1736-1757. doi:10.1002/esp.3947
568 Gallen, S.F., 2018. Lithologic controls on landscape dynamics and aquatic species evolution in post-
569 orogenic mountains. Earth and Planetary Science Letters 493, 150-160.
570 doi:10.1016/j.epsl.2018.04.029
571 Giachetta, E., Refice, A., Capolongo, D., Gasparini, N.M., Pazzaglia, F.J., 2014. Orogen-scale drainage
572 network evolution and response to erodibility changes: insights from numerical experiments. Earth
573 Surface Processes and Landforms 39, 1259-1268. doi:10.1002/esp.3579
574 Gokceoglu, C., Aksoy, H., 2000. New approaches to the characterization of clay-bearing, densely
575 jointed and weak rock masses. Engineering Geology 58, 1-23. doi:10.1016/s0013-7952(00)00032-6
576 Goktan, R.M., Gunes, N., 2005. A comparative study of Schmidt hammer testing procedures with
577 reference to rock cutting machine performance prediction. International Journal of Rock Mechanics
578 and Mining Sciences 42, 466-472. doi:10.1016/j.ijrmms.2004.12.002
579 Goudie, A.S., 2006. The Schmidt Hammer in geomorphological research. Progress in Physical
580 Geography: Earth and Environment 30, 703-718. doi:10.1177/0309133306071954
581 Hughes, P.D., Gibbard, P.L., Woodward, J.C., 2004. Quaternary glaciation in the Atlas Mountains of
582 North Africa, in: Ehlers, J., Gibbard, P.L. (Eds.), Developments in Quaternary Sciences. Elsevier, pp.
583 255-260. doi:10.1016/S1571-0866(04)80131-3
584 Kahraman, S., Fener, M., Gunaydin, O., 2002. Predicting the Schmidt hammer values of in-situ intact
585 rock from core sample values. International Journal of Rock Mechanics and Mining Sciences 39, 395-
586 399. doi:10.1016/S1365-1609(02)00028-X
587 Kahraman, S., Fener, M., Kozman, E., 2012. Predicting the compressive and tensile strength of rocks
588 from indentation hardness index. J S Afr I Min Metall 112, 331-339.
589 Karakus, M., Kumral, M., Kilic, O., 2005. Predicting elastic properties of intact rocks from index tests
590 using multiple regression modelling. International Journal of Rock Mechanics and Mining Sciences
591 42, 323-330. doi:10.1016/j.ijrmms.2004.08.005
592 Katz, O., Reches, Z., Roegiers, J.-C., 2000. Evaluation of mechanical rock properties using a Schmidt
593 Hammer. International Journal of rock mechanics and mining sciences 37, 723-728.
594 doi:10.1016/S1365-1609(00)00004-6
595 Lague, D., 2014. The stream power river incision model: evidence, theory and beyond. Earth Surface
596 Processes and Landforms 39, 38-61. doi:10.1002/esp.3462
597 Mather, A.E., Stokes, M., 2018. Bedrock structural control on catchment-scale connectivity and
598 alluvial fan processes, High Atlas Mountains, Morocco. Geological Society, London, Special
599 Publications 440, 103-128. doi:10.1144/sp440.15

Nazir, R., Momeni, E., Armaghani, D.J., Amin, M.M., 2013. Correlation between unconfined compressive strength and indirect tensile strength of limestone rock samples. Electronic Journal of Geotechnical Engineering 18, 1737-1746.
Perne, M., Covington, M.D., Thaler, E.A., Myre, J.M., 2017. Steady state, erosional continuity, and the topography of landscapes developed in layered rocks. Earth Surf. Dynam. 5, 85-100. doi:10.5194/esurf-5-85-2017
Perron, J.T., Royden, L., 2013. An integral approach to bedrock river profile analysis. Earth Surface Processes and Landforms 38, 570-576. doi:10.1002/esp.3302
Pye, K., Goudie, A.S., Watson, A., 1986. Petrological influence on differential weathering and inselberg development in the Kora area of central Kenya. Earth Surface Processes and Landforms 11, 41-52. doi:10.1002/esp.3290110106
Roy, S.G., Koons, P.O., Upton, P., Tucker, G.E., 2015. The influence of crustal strength fields on the patterns and rates of fluvial incision. Journal of Geophysical Research: Earth Surface 120, 275-299. doi:10.1002/2014jf003281
Saadi, M., Hilali, E.A., Bensaid, M., Boudda, A., Dahmani, M., 1985. Carte Géologique du Maroc Notes et mémoires (Morocco. Service Géologique). Editions du Service Géologique du Maroc.
Schanz, S.A., Montgomery, D.R., 2016. Lithologic controls on valley width and strath terrace formation. Geomorphology 258, 58-68. doi:10.1016/j.geomorph.2016.01.015
Schwanghart, W., Scherler, D., 2014. Short Communication: TopoToolbox 2 – MATLAB-based software for topographic analysis and modeling in Earth surface sciences. Earth Surface Dynamics 2, 1-7. doi:10.5194/esurf-2-1-2014
Sklar, L.S., Dietrich, W.E., 2001. Sediment and rock strength controls on river incision into bedrock. Geology 29, 1087-1090. doi:10.1130/0091-7613(2001)029<1087:sarsco>2.0.co;2
Stock, J.D., Montgomery, D.R., 1999. Geologic constraints on bedrock river incision using the stream power law. Journal of Geophysical Research. B 104, 4983-4993. doi:10.1029/98JB02139
Stokes, M., Mather, A.E., Belfoul, M., Faik, F., Bouzid, S., Geach, M.R., Cunha, P.P., Boulton, S.J., Thiel, C., 2017. Controls on dryland mountain landscape development along the NW Saharan desert margin: Insights from Quaternary river terrace sequences (Dadès River, south-central High Atlas, Morocco). Quaternary Science Reviews 166, 363-379. doi:10.1016/j.quascirev.2017.04.017
Strong, C.M., Attal, M., Mudd, S.M., Sinclair, H.D., 2019. Lithological control on the geomorphic evolution of the Shillong Plateau in Northeast India. Geomorphology 330, 133-150. doi:10.1016/j.geomorph.2019.01.016
Teixell, A., Arboleya, M.-L., Julivert, M., Charroud, M., 2003. Tectonic shortening and topography in the central High Atlas (Morocco). Tectonics 22, n/a-n/a. doi:10.1029/2002tc001460
Thaler, E.A., Covington, M.D., 2016. The influence of sandstone caprock material on bedrock channel steepness within a tectonically passive setting: Buffalo National River Basin, Arkansas, USA. Journal of Geophysical Research: Earth Surface 121, 1635-1650. doi:10.1002/2015jf003771
Whipple, K.X., Tucker, G.E., 1999. Dynamics of the stream-power river incision model: Implications for height limits of mountain ranges, landscape response timescales, and research needs. Journal of Geophysical Research: Solid Earth 104, 17661-17674. doi:10.1029/1999jb900120
Willett, S.D., McCoy, S.W., Perron, J.T., Goren, L., Chen, C.Y., 2014. Dynamic reorganization of river basins. Science 343, 1248765. doi:10.1126/science.1248765
Willett, S.D., Slingerland, R., Hovius, N., 2001. Uplift, Shortening, and Steady State Topography in Active Mountain Belts. American Journal of Science 301, 455-485. doi:10.2475/ajs.301.4-5.455
Wobus, C., Whipple, K.X., Kirby, E., Snyder, N., Johnson, J., Spyropolou, K., Crosby, B., Sheehan, D., 2006. Tectonics from topography: Procedures, promise, and pitfalls. Geological Society of America Special Papers 398, 55-74. doi:10.1130/2006.2398(04)
Yanites, B.J., Becker, J.K., Madritsch, H., Schnellmann, M., Ehlers, T.A., 2017. Lithologic Effects on Landscape Response to Base Level Changes: A Modeling Study in the Context of the Eastern Jura Mountains, Switzerland. Journal of Geophysical Research: Earth Surface 122, 2196-2222. doi:10.1002/2016jf004101